# Two and three-dimensional boundary element formulations of compressible isotropic, transversely isotropic and orthotropic viscoelastic layers of arbitrary thickness, applied to the rolling resistance of rigid cylinders and spheres

Gérard-Philippe Zéhil[a,*], Henri P. Gavin[a]

[a]*Department of Civil and Environmental Engineering, Duke University, 121 Hudson Hall, Box 90287, Research Drive, Durham, NC 27708-0287, United States*

**Abstract**

New two-dimensional and three-dimensional boundary element formulations of *compressible* viscoelastic layers of arbitrary thickness are presented in this work. The formulations are derived in increasing order of complexity for: (i) compressible isotropic layers, (ii) transversely isotropic layers, and (iii) fully orthotropic layers. It is further shown that existing 2D and 3D models for *incompressible* isotropic layers may be regarded as particular instances of case (i). The proposed formulations are based on Fourier series and support any linear viscoelastic material model characterized by general frequency-domain master-curves. These approaches result in a compliance matrix for the layer's upper boundary, which includes the effects of steady-state motion. This characterization may be used as a component in various problem settings to generate sequences of high fidelity solutions for varying parameters. The proposed modeling techniques are applied, in combination with appropriate contact solvers, to the rolling resistance of rigid cylinders and spheres on compressible isotropic, transversely isotropic and orthotropic layers. The latter case reveals that the dissipated power varies with the direction of motion, which suggests new ways of optimizing the level of damping in various engineering applications of very high impact. Interesting lateral viscoelastic effects resulting from material asymmetry are unveiled. These phenomena could be harnessed to achieve smooth and 'invisible' guides across three-dimensional viscoelastic surfaces, and hence suggest new ways of controlling trajectories, with a broad range of potential applications.

*Keywords:* Rolling resistance, boundary element method, compressible viscoelasticity, orthotropic layer, Fourier series.

## 1. Motivations and background

A three-dimensional boundary element formulation of an *incompressible* viscoelastic layer of arbitrary thickness was proposed by Zéhil and Gavin (2013b). This formulation was applied, in combination with appropriate rolling/sliding contact algorithms (Zéhil and Gavin, 2013a), to determine the resistance incurred by a rigid sphere rolling, in steady-state, on such a layer.

The authors' interest in rolling resistance initially stems from the exploration of new damping principles suitable for the seismic isolation of critical facilities. A recent study conducted by Harvey and Gavin (2013) on a Ball-N-Cone$^{TM}$rolling isolation bearing (WorkSafe Technologies, 2012) addresses the benefits of damping in rolling isolation systems. In order to limit the peak acceleration levels to which sensitive equipment may be subjected to during the course of an earthquake, higher levels of 'soft' damping can be achieved by increasing the resistance to rolling or sliding of their seismic isolation platforms. In practice, this damping principle can be implemented by inserting a dampening material between contacting components of the isolation system, in relative motion with respect to each other. For instance, in the case of rolling isolation bearings, viscoelastic rubber sheets can be inserted between the rigid roller (e.g. a sphere) and the hard surfaces on which the rolling occurs (e.g. 'dished' or bowl-shaped steel plates).

*Corresponding author

*Email address:* gerard.zehil@duke.edu (Gérard-Philippe Zéhil)

An early and approximate closed-form expression for the rolling resistance $R_r$ incurred by a rigid sphere rolling on a *compressible* viscoelastic half-space was derived by Greenwood and Tabor (1958) who integrated, under the small strain assumption, the horizontal projection of the stationary normal stress distribution, as given by Hertz (1881), over the front half of the contact 'disk', and evaluated its work per unit distance of rolling. The proposed expression for rolling resistance is in good agreement with experimental results presented by the authors for spheres moving slower than at 1 cm/s under mean contact pressures below 2.76 MPa (i.e. 400 lb.in$^{-2}$). This expression may be re-written as follows

$$R_r \approx \alpha_{GT} \left(\frac{3^4}{4^7}\right)^{\frac{1}{3}} \left(\frac{1-\nu^2}{E}\right)^{\frac{1}{3}} \frac{P^{\frac{4}{3}}}{R^{\frac{2}{3}}}, \tag{1}$$

where $P$ is the vertical load supported by the rolling sphere, and $R$ stands for its radius. Young's modulus $E$ and Poisson's ratio $\nu$ of the layer's material, as well as the loss fraction $\alpha_{GT}$ of the input deformation energy are taken as constants. Flom and Bueche (1959) proposed an alternative simplified theory accounting for the influence of rolling speed and resulting in expressions that otherwise confirm, for intermediate values of the dynamic loss factor (known as $\tan\delta$), the dependencies of rolling resistance predicted by equation (1) on the vertical load $P$, the radius of the sphere $R$ and the layer's stiffness. These expressions may be written in the generic form

$$R_r \approx \alpha_{FB} \left(\frac{1-\nu^2}{E}\right)^{\frac{1}{3}} \frac{P^{\frac{4}{3}}}{R^{\frac{2}{3}}}, \tag{2}$$

where, as noted by Lakes (2009), $\alpha_{FB}$ depends on $\tan\delta$ and therefore on the material parameters of the layer and on the frequency of rolling. Based on the simplifying assumption that the dynamic contact region has a similar size to that given by the static solution of Hertz, Lakes also noted that an upper bound for the viscoelastic rolling resistance of a rigid sphere is given by

$$R_r \approx \left(\frac{3}{4}\right)^{\frac{1}{3}} \left(\frac{1-\nu^2}{E}\right)^{\frac{1}{3}} \frac{P^{\frac{4}{3}}}{R^{\frac{2}{3}}}, \tag{3}$$

where $E$ is interpreted as a dynamic modulus at a circular frequency $\omega$, proportional to $V_s/R$. Expressions (1)-(3) are furthermore consistent in predicting that rolling resistance decreases with Young's modulus and that it is maximized by a Poisson ratio of zero. Hence, based on this simple and qualitative reasoning, it may be expected that relatively soft and compressible layers, with a Poisson ratio that it close to zero, would yield higher levels of resistance and damping than harder layers or layers made of incompressible materials ($\nu \approx 0.5$) such as rubbers.

The boundary element formulation presented in Zéhil and Gavin (2013b) applies to *incompressible* and *isotropic* layers, which is practically the case of most rubber-like materials. Compressible materials are however characterized by one additional frequency-dependent complex parameter, i.e. the complex Poisson ratio $\nu^*(\omega)$, and can not be modeled with this formulation. Extending the boundary element formulation to *compressible* layers is therefore needed. In section 4, a compressible isotropic formulation is derived, in three dimensions, to answer this first need. This derivation is somewhat akin to that proposed by Persson (2001) based on Fourier transforms and applied in a simplified approach to the rolling resistance of hard cylinders and sphere on a viscoelastic layer (Persson, 2010). A two-dimensional formulation in plane strain is deduced in section 7 to complement the incompressible formulations proposed by Qiu (2006, 2009).

Moving further, one may think of cork as an example of relatively soft material characterized by a Poisson ratio that is close to zero. In fact this material is used as a stopper for wine bottles because it shows very little lateral expansion when it is compressed. However, cork does not behave isotropically. Indeed, its prismatic cells are packed in columns in the radial direction, which constitutes a direction of symmetry of the cellular structure. Cork may therefore be modeled as a transversely isotropic medium (e.g. Rosa and Fortes, 1991). In order to achieve accurate rolling resistance predictions on viscoelastic materials such as cork, with different mechanical characteristics in the out-of-plane direction, the boundary element formulation must further be extended to polar anisotropic layers. This additional need is addressed in section 5 where a three-dimensional transversely isotropic formulation is derived. This formulation is specialized further to plane strain in section 8.

On the other hand, a hard-wearing layer cannot be too soft. Hence, there seems to be a tradeoff between high resistance to rolling and durability. Given the need to achieve optimal levels of damping under specific conditions (of seismic hazard for instance) while maintaining suitable service life expectancies, the future use of specially designed

layers made of viscoelastic *metamaterials* cannot be excluded and should therefore be prepared. Man-made materials, such as auxetic composites made of rubber-filled re-entrant honeycombs for instance, are often characterized by different mechanical properties in three orthogonal directions. Predicting the resistance of such materials to rolling and sliding would ultimately require extending the boundary element formulation to fully orthotropic layers. This need is fully addressed in section 6.

## 2. Common setting

The different cases considered in this work share a common setting, which is illustrated in figure 1: a mechanical load is translated at constant speed $V_s$, in direction $x$, on a viscoelastic layer of arbitrary thickness $H$, attached to a rigid backing. The load is periodic in directions $x$ and $y$, with periods $L_x$ and $L_y$, respectively. The coordinate system $Ox'y'z'$ is fixed while $Oxyz$ moves with the load.

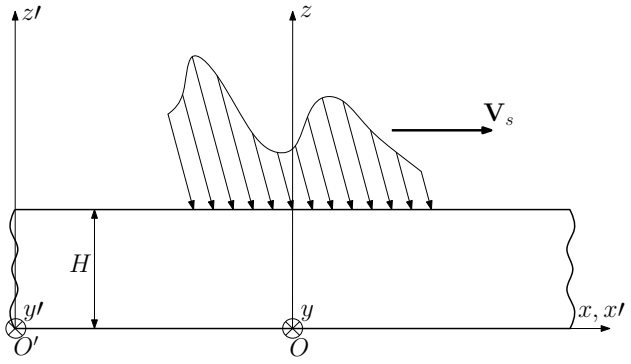


Figure 1: General model and coordinate systems

## 3. A brief review of 3D linear viscoelasticity

Linear elasticity corresponds to a time-independent behavioral material model characterized by the constitutive equation below, also known as Hook's law, written in indicial notation as

$$\sigma_{ij} = C_{ijkl}\epsilon_{kl}, \tag{4}$$

where $\sigma_{ij}$, $\epsilon_{ij}$ and $C_{ijkl}$ are components of the second order stress tensor, the small-strain tensor, and the fourth order elasticity tensor, respectively.

Alternatively, linear viscoelasticity is characterized by the dependence of the elasticity tensor on time. The state of stress in a linear viscoelastic material, subjected to a strain history of the form $\epsilon_{kl}(t) = \bar{\epsilon}_{kl}\mathcal{H}(t)$, where $\bar{\epsilon}_{kl}$ are constant strain components and $\mathcal{H}(.)$ designates the Heaviside unit step function, is given by

$$\sigma_{ij}(t) = C_{ijkl}(t)\,\bar{\epsilon}_{kl}, \qquad t \geq 0. \tag{5}$$

The linear viscoelastic response to a more general strain history (on $t \geq 0$) can be deduced, using the principle of superposition, by convolution of (5), in the form of a hereditary integral (e.g. Flügge, 1975; Lakes, 2009), i.e.

$$\sigma_{ij}(t) = \int_0^t C_{ijkl}(t-\tau)\,\frac{d\epsilon_{kl}}{d\tau}d\tau. \tag{6}$$

Taking the Fourier transform of (6), frequency-domain linear viscoelasticity is characterized under cyclic loading by

$$\hat{\sigma}_{ij}(\omega) = C^*_{ijkl}(\omega)\,\hat{\epsilon}_{kl}(\omega), \tag{7}$$

where the circumflex refers to complex-valued functions of the angular frequency $\omega$, and $C^*_{ijkl}(\omega) = i\omega\hat{C}_{ijkl}(\omega)$, with $i^2 = -1$, are complex elastic moduli. Equation (7) can also be written, using the Voigt notation, in the following form

$$\hat{\boldsymbol{\sigma}}(\omega) = \mathbf{C}^*(\omega)\,\hat{\boldsymbol{\epsilon}}(\omega), \tag{8}$$

where $\hat{\boldsymbol{\sigma}}(\omega) = \langle\hat{\sigma}_{11}, \hat{\sigma}_{22}, \hat{\sigma}_{33}, \hat{\sigma}_{23}, \hat{\sigma}_{13}, \hat{\sigma}_{12}\rangle^T$, $\hat{\boldsymbol{\epsilon}}(\omega) = \langle\hat{\epsilon}_{11}, \hat{\epsilon}_{22}, \hat{\epsilon}_{33}, \hat{\gamma}_{23}, \hat{\gamma}_{13}, \hat{\gamma}_{12}\rangle^T$ with $\hat{\gamma}_{kl} = 2\hat{\epsilon}_{kl}$, and $\mathbf{C}^*(\omega)$ is a $6\times6$ complex-valued elasticity matrix. In particular, orthogonally isotropic materials are characterized by nine independent elastic moduli (e.g. Boresi and Schmidt, 2003; Lekhnitskiĭ, 1963; Rand et al., 2005; Sadd, 2009; Slawinski, 2010), which may be selected among the ones populating the *symmetric* elasticity matrix below, written in the principal axes of orthotropy

$$\mathbf{C}^*(\omega) = \begin{bmatrix} \frac{E^*_1}{\Delta^*}\left(1-\nu^*_{23}\nu^*_{32}\right) & \frac{E^*_1}{\Delta^*}\left(\nu^*_{21}+\nu^*_{23}\nu^*_{31}\right) & \frac{E^*_1}{\Delta^*}\left(\nu^*_{31}+\nu^*_{32}\nu^*_{21}\right) & 0 & 0 & 0 \\ \frac{E^*_2}{\Delta^*}\left(\nu^*_{12}+\nu^*_{13}\nu^*_{32}\right) & \frac{E^*_2}{\Delta^*}\left(1-\nu^*_{13}\nu^*_{31}\right) & \frac{E^*_2}{\Delta^*}\left(\nu^*_{32}+\nu^*_{31}\nu^*_{12}\right) & 0 & 0 & 0 \\ \frac{E^*_3}{\Delta^*}\left(\nu^*_{13}+\nu^*_{12}\nu^*_{23}\right) & \frac{E^*_3}{\Delta^*}\left(\nu^*_{23}+\nu^*_{21}\nu^*_{13}\right) & \frac{E^*_3}{\Delta^*}\left(1-\nu^*_{21}\nu^*_{12}\right) & 0 & 0 & 0 \\ 0 & 0 & 0 & G^*_{23} & 0 & 0 \\ 0 & 0 & 0 & 0 & G^*_{13} & 0 \\ 0 & 0 & 0 & 0 & 0 & G^*_{12} \end{bmatrix}, \tag{9}$$

where $E^*_i$ is Young's modulus along the $i$-axis, $\nu_{ij}$ refers to Poisson's ratio corresponding to a contraction along the $j$-axis upon extension in direction $i$, and $G_{ij}$ is the complex shear modulus in the $ij$-plane. The shorthand parameter $\Delta^*(\omega)$ is defined as

$$\Delta^*(\omega) = 1 - \nu^*_{12}\nu^*_{21} - \nu^*_{13}\nu^*_{31} - \nu^*_{23}\nu^*_{32} - \nu^*_{12}\nu^*_{23}\nu^*_{31} - \nu^*_{13}\nu^*_{32}\nu^*_{21}. \tag{10}$$

A transversely isotropic material whose properties are symmetric about the 3-axis is characterized by five independent elastic moduli, such that $\mathbf{C}^*(\omega)$ is a *symmetric* matrix of the form

$$\mathbf{C}^*(\omega) = \begin{bmatrix} \frac{1-\nu^*_{LT}\nu^*_{TL}}{E^*_L E^*_T \Gamma^*} & \frac{\nu^*_T+\nu^*_{LT}\nu^*_{TL}}{E^*_L E^*_T \Gamma^*} & \frac{\nu^*_{LT}\left(1+\nu^*_T\right)}{E^*_L E^*_T \Gamma^*} & 0 & 0 & 0 \\ \frac{\nu^*_T+\nu^*_{LT}\nu^*_{TL}}{E^*_L E^*_T \Gamma^*} & \frac{1-\nu^*_{LT}\nu^*_{TL}}{E^*_L E^*_T \Gamma^*} & \frac{\nu^*_{LT}\left(1+\nu^*_T\right)}{E^*_L E^*_T \Gamma^*} & 0 & 0 & 0 \\ \frac{\nu^*_{TL}\left(1+\nu^*_T\right)}{E^{*2}_T \Gamma^*} & \frac{\nu^*_{TL}\left(1+\nu^*_T\right)}{E^{*2}_T \Gamma^*} & \frac{1-\nu^{*2}_T}{E^{*2}_T \Gamma^*} & 0 & 0 & 0 \\ 0 & 0 & 0 & G^*_{LT} & 0 & 0 \\ 0 & 0 & 0 & 0 & G^*_{LT} & 0 \\ 0 & 0 & 0 & 0 & 0 & \frac{E^*_T}{2\left(1+\nu^*_T\right)} \end{bmatrix}, \tag{11}$$

where the subscripts $T$ and $L$ refer to the "transverse" plane of isotropy (i.e. the 12-plane) and the "longitudinal" axis of symmetry (i.e. the 3-axis), respectively. The shorthand parameter $\Gamma^*(\omega)$ is defined as

$$\Gamma^*(\omega) = \frac{\left(1+\nu^*_T\right)\left(1-\nu^*_T-2\nu^*_{TL}\nu^*_{LT}\right)}{E^{*2}_T E^*_L}. \tag{12}$$

In the isotropic case, $C^*_{ijkl}$ are given in terms of two complex-valued Lamé functions $\mu^*(\omega) = i\omega\hat{\mu}(\omega)$ and $\lambda^*(\omega) = i\omega\hat{\lambda}(\omega)$, as

$$C^*_{ijkl}(\omega) = \left(\delta_{ik}\delta_{jl} + \delta_{il}\delta_{jk}\right)\mu^*(\omega) + \delta_{ij}\delta_{kl}\lambda^*(\omega). \tag{13}$$

Alternatively, traditional "engineering" quantities, such as the complex Young's modulus $E^*(\omega)$ and Poisson's ratio $\nu^*(\omega)$, may be substituted to Lamé's functions in (13), with

$$\mu^*(\omega) = \frac{E^*(\omega)}{2\left(1+\nu^*(\omega)\right)} \quad \text{and} \quad \lambda^*(\omega) = \frac{E^*(\omega)\,\nu^*(\omega)}{\left(1+\nu^*(\omega)\right)\left(1-2\nu^*(\omega)\right)}. \tag{14}$$

When (13) applies, the constitutive relation in (7) can be split into isochoric and volumetric parts, involving the complex shear modulus $G^*(\omega) = \mu^*(\omega)$, and the complex bulk modulus $K^*(\omega) = (2/3)\mu^*(\omega) + \lambda^*(\omega)$, respectively, i.e.

$$\hat{\sigma}'_{ij}(\omega) = 2G^*(\omega)\,\hat{\epsilon}'_{ij}(\omega), \tag{15}$$

$$\hat{\sigma}_o(\omega) = K^*(\omega)\,\phi(\omega), \tag{16}$$

where primed quantities correspond to deviator components, $\phi(\omega) = \hat{\epsilon}_{kk}(\omega)$ and $\hat{\sigma}_o(\omega) = \hat{\sigma}_{kk}(\omega)/3$. Expressions (15) and (16) are typically used in experimental setups to effectively determine $G^*(\omega)$ and $K^*(\omega)$ in a wide frequency range (e.g. Pritz, 2000). These are related to the engineering moduli by

$$E^*(\omega) = \frac{9K^*(\omega)\,G^*(\omega)}{3K^*(\omega) + G^*(\omega)} \quad \text{and} \quad \nu^*(\omega) = \frac{1}{2}\left(\frac{3K^*(\omega) - 2G^*(\omega)}{3K^*(\omega) + G^*(\omega)}\right). \tag{17}$$

## 4. Three-dimensional isotropic formulation

A three-dimensional boundary element formulation for an *incompressible* layer of finite thickness was proposed by Zéhil and Gavin (2013b). The derivation presented here follows somewhat similar steps, adapted to the context of a *compressible* layer. Designating by $\mathbf{f}$ any general field in the continuum of the layer, and by $\mathbf{u} =< u, v, w >^T$ the displacement vector field, specific boundary conditions for the layer, of spatial periods $L_x$ and $L_y$, in directions $x$ and $y$ respectively, can be expressed as

$$\mathbf{u}(x, y, z = 0) = \mathbf{0}, \qquad \forall\,(x, y), \tag{18}$$

$$\mathbf{f}\left(x + pL_x, y + qL_y, z\right) = \mathbf{f}(x, y, z), \qquad \forall\,(x, y) \in \mathbb{R}^2, \forall z \in [0, H] \text{ and } \forall\,(p, q) \in \mathbb{Z}^2. \tag{19}$$

Coordinate sytems $Oxyz$ and $O'x'y'z'$ are related by $x = x' - V_s t$, $y = y'$ and $z = z'$. Consequently, material time-derivatives write

$$\frac{d}{dt} = -V_s\frac{\partial}{\partial x} \quad \text{and} \quad \frac{d^2}{dt^2} = V_s^2\frac{\partial^2}{\partial x^2}. \tag{20}$$

Let $\rho$ be the material's density. In the absence of volume forces, equilibrium equations in the continuum of the layer are expressed in $Oxyz$, by means of (20) using tensor notation as

$$\rho V_s^2\frac{\partial^2\mathbf{u}}{\partial x^2} = \mathbf{div}(\boldsymbol{\sigma}). \tag{21}$$

Individual components of all fields are expanded into Fourier series in the spatial variables $x$ and $y$. The expansions are subsequently written in terms of $x'$, $y'$ and $t$. This is shown below on a generic scalar quantity $f(x, y, z)$ of the problem

$$f(x, y, z) = \sum_{m,n=-\infty}^{+\infty} f_{mn}(z)e^{i\nu_x x}e^{i\nu_y y} = \sum_{m,n=-\infty}^{+\infty} f_{mn}(z)e^{i\nu_x x'}e^{i\nu_x y'}e^{i\omega_m t}, \tag{22}$$

where $\nu_x = 2\pi m/L_x$, $\nu_y = 2\pi n/L_y$ and $\omega_m = -2\pi m V_s/L_x$. Corresponding Fourier coefficients are given by

$$f_{mn}(z) = \frac{1}{L_x L_y}\int_{y=0}^{L_y}\int_{x=0}^{L_x} f(x, y, z)e^{-i\nu_x x}e^{-i\nu_y y}dxdy. \tag{23}$$

Substituting expansion (22) into the hereditary integral in (6) for $\sigma_{ij}(t)$ and $\epsilon_{kl}(\tau)$, then integrating over spatial periods while using the orthogonality property of complex exponentials yields a behavioral formulation in terms of Fourier coefficients, i.e.

$$\sigma_{ij_{mn}}(z) = C^*_{ijkl_m}\epsilon_{kl_{mn}}(z), \tag{24}$$

where $C^*_{ijkl_m} = C^*_{ijkl}(\omega_m)$, with no summation implied on indices $m$ and $n$. Transcribed into Voigt's notation, equation (24) becomes

$$\boldsymbol{\sigma}_{mn}(z) = \mathbf{C}^*_m\boldsymbol{\epsilon}_{mn}(z), \tag{25}$$

where $\boldsymbol{\sigma}_{mn}(z) = \langle\sigma_{11_{mn}}, \sigma_{22_{mn}}, \sigma_{33_{mn}}, \sigma_{23_{mn}}, \sigma_{13_{mn}}, \sigma_{12_{mn}}\rangle^T$, $\boldsymbol{\epsilon}_{mn}(z) = \langle\epsilon_{11_{mn}}, \epsilon_{22_{mn}}, \epsilon_{33_{mn}}, \gamma_{23_{mn}}, \gamma_{13_{mn}}, \gamma_{12_{mn}}\rangle^T$ with $\gamma_{kl_{mn}} = 2\epsilon_{kl_{mn}}$, and $\mathbf{C}^*_m = \mathbf{C}^*(\omega_m)$. Expressions (24) and (25) may be compared to their (single-variable) Fourier transform counterparts given in (7) and (8), respectively. For brevity, explicit references to the dependence of Fourier coefficients

on the spatial variable $z$ will be omitted in the following. In the isotropic case, substituting expressions (17) into (13) then (13) into (24), yields

$$\sigma_{ij_{mn}} = \frac{E_m^*}{1+\nu_m^*}\left(\epsilon_{ij_{mn}} + \frac{\nu_m^*}{1-2\nu_m^*}\epsilon_{kk_{mn}}\delta_{ij}\right). \tag{26}$$

Expansion (22) can also be plugged into the equilibrium equations in (21), which, following a procedure similar to the one described above, yields a system of linear ordinary differential equations (ODE's) relating stress and displacement Fourier coefficients

$$-\rho V_s^2 \nu_x^2 u_{mn} = i\nu_x \sigma_{xx_{mn}} + i\nu_y \tau_{xy_{mn}} + \dot{\tau}_{xz_{mn}}, \tag{27}$$

$$-\rho V_s^2 \nu_x^2 v_{mn} = i\nu_x \tau_{xy_{mn}} + i\nu_y \sigma_{yy_{mn}} + \dot{\tau}_{yz_{mn}}, \tag{28}$$

$$-\rho V_s^2 \nu_x^2 w_{mn} = i\nu_x \tau_{xz_{mn}} + i\nu_y \tau_{yz_{mn}} + \dot{\sigma}_{zz_{mn}}. \tag{29}$$

Further, differentiating expression (22) for the displacements $(u, v, w)$ with respect to the spatial variables $(x, y, z)$ and eliminating strain coefficients $\epsilon_{ij_{mn}}$ in (26) results in additional ODE's relating Fourier coefficients of displacements and stresses

$$\sigma_{xx_{mn}} = \frac{E_m^*}{(1+\nu_m^*)(1-2\nu_m^*)}\left[(1-\nu_m^*)\, i\nu_x u_{mn} + \nu_m^*\left(i\nu_y v_{mn} + \dot{w}_{mn}\right)\right], \tag{30}$$

$$\sigma_{yy_{mn}} = \frac{E_m^*}{(1+\nu_m^*)(1-2\nu_m^*)}\left[(1-\nu_m^*)\, i\nu_y v_{mn} + \nu_m^*\left(i\nu_x u_{mn} + \dot{w}_{mn}\right)\right], \tag{31}$$

$$\sigma_{zz_{mn}} = \frac{E_m^*}{(1+\nu_m^*)(1-2\nu_m^*)}\left[(1-\nu_m^*)\, \dot{w}_{mn} + \nu_m^*\left(i\nu_x u_{mn} + i\nu_y v_{mn}\right)\right], \tag{32}$$

$$\tau_{xy_{mn}} = \frac{E_m^*}{2(1+\nu_m^*)}\left(i\nu_y u_{mn} + i\nu_x v_{mn}\right), \tag{33}$$

$$\tau_{xz_{mn}} = \frac{E_m^*}{2(1+\nu_m^*)}\left(i\nu_x w_{mn} + \dot{u}_{mn}\right), \tag{34}$$

$$\tau_{yz_{mn}} = \frac{E_m^*}{2(1+\nu_m^*)}\left(i\nu_y w_{mn} + \dot{v}_{mn}\right), \tag{35}$$

where the up dot denotes the derivative with respect to $z$. For a given couple of Fourier indices $(m, n)$, a complex-valued state vector $\mathbf{q}_{mn}(z)$ is defined, as follows

$$\mathbf{q}_{mn}(z) = \left\langle \mathbf{d}_{mn}^T(z), \mathbf{f}_{mn}^T(z)\right\rangle^T \tag{36}$$

where $\mathbf{d}_{mn}(z) = \langle w_{mn}(z), u_{mn}(z), v_{mn}(z)\rangle^T$ and $\mathbf{f}_{mn}(z) = \left\langle \sigma_{zz_{mn}}(z), \tau_{xz_{mn}}(z), \tau_{yz_{mn}}(z)\right\rangle^T$. Eliminating the remaining quantities from equations (27)-(35) results in a reduced system of linear ODE's of the form

$$\dot{\mathbf{q}}_{mn}(z) = \mathbf{A}_{mn}\mathbf{q}_{mn}(z) \tag{37}$$

where the $6\times 6$ complex-valued matrix $\mathbf{A}_{mn}$ is given by

$$\mathbf{A}_{mn} = \begin{bmatrix} 0 & -i\xi^*\nu_x & -i\xi^*\nu_y & \zeta^* & 0 & 0 \\ -i\nu_x & 0 & 0 & 0 & G_m^{*\,-1} & 0 \\ -i\nu_y & 0 & 0 & 0 & 0 & G_m^{*\,-1} \\ -\rho V_s^2\nu_x^2 & 0 & 0 & 0 & -i\nu_x & -i\nu_y \\ 0 & \beta_x^* & \beta_{xy}^* & -i\xi^*\nu_x & 0 & 0 \\ 0 & \beta_{xy}^* & \beta_y^* & -i\xi^*\nu_y & 0 & 0 \end{bmatrix}. \tag{38}$$

Shorthand parameters appearing in (38) are defined below

$$\beta_x^* = \frac{E_m^*}{2(1+\nu_m^*)}\left(\frac{2\nu_x^2}{1-\nu_m^*} + \nu_y^2\right) - \rho V_s^2\nu_x^2, \tag{39}$$

$$\beta_y^* = \frac{E_m^*}{2\,(1+\nu_m^*)}\left(\frac{2\nu_y^2}{1-\nu_m^*}+\nu_x^2\right)-\rho V_s^2\nu_x^2, \tag{40}$$

$$\beta_{xy}^* = \frac{E_m^*\nu_x\nu_y}{2\,(1-\nu_m^*)},\quad G_m^* = \frac{E_m^*}{2\,(1+\nu_m^*)}, \tag{41}$$

$$\zeta^* = \frac{(1+\nu_m^*)\,(1-2\nu_m^*)}{E_m^*\,(1-\nu_m^*)}\quad\text{and}\quad \xi^* = \frac{\nu_m^*}{1-\nu_m^*}. \tag{42}$$

The remaining steps correspond to an inverse Fourier analysis, i.e. to the formation of a compliance matrix $\mathbf{C}$ fully characterizing the mechanical behavior of the layer's upper boundary, in the physical space. These steps, are identical to those described by Zéhil and Gavin (2013b) in the context of an incompressible layer. Briefly, the solution to system (37) is written in the following form

$$\begin{bmatrix}\mathbf{d}_{mn}(z)\\ \mathbf{f}_{mn}(z)\end{bmatrix} = \begin{bmatrix}\mathbf{T}_{mn,11}(z) & \mathbf{T}_{mn,12}(z)\\ \mathbf{T}_{mn,21}(z) & \mathbf{T}_{mn,22}(z)\end{bmatrix}\times\begin{bmatrix}\mathbf{d}_{mn}(0)\\ \mathbf{f}_{mn}(0)\end{bmatrix}, \tag{43}$$

where $\mathbf{T}_{mn}(z) = \exp(\mathbf{A}_{mn}z)$ is the complex matrix exponential of $\mathbf{A}_{mn}z$. Accounting for the boundary conditions on displacements at the bottom of the layer, i.e. $\mathbf{d}_{mn}(0) = \mathbf{0}$, Fourier coefficients of displacements and stresses at $z = H$ can be related explicitly

$$\mathbf{d}_{mn}(H) = \mathbf{T}_{mn,12}(H)\mathbf{T}_{mn,22}^{-1}(H)\mathbf{f}_{mn}(H). \tag{44}$$

The upper boundary of the layer is discretized into nodes with nodal spacings $a_x$ and $a_y$ in directions $x$ and $y$ respectively. The nodal displacement vector $\mathbf{D} = \left\langle \mathbf{W}^T, \mathbf{U}^T, \mathbf{V}^T\right\rangle^T$ is related to the nodal force vector $\mathbf{F} = \left\langle \mathbf{F_W}^{\mathbf{T}}, \mathbf{F_U}^{\mathbf{T}}, \mathbf{F_V}^{\mathbf{T}}\right\rangle^{\mathbf{T}}$ through a boundary-element compliance matrix $\mathbf{C}$ as

$$\begin{bmatrix}\mathbf{C}_{WW} & \mathbf{C}_{WU} & \mathbf{C}_{WV}\\ \mathbf{C}_{UW} & \mathbf{C}_{UU} & \mathbf{C}_{UV}\\ \mathbf{C}_{VW} & \mathbf{C}_{VU} & \mathbf{C}_{VV}\end{bmatrix}\begin{bmatrix}\mathbf{F}_W\\ \mathbf{F}_U\\ \mathbf{F}_V\end{bmatrix} = \begin{bmatrix}\mathbf{W}\\ \mathbf{U}\\ \mathbf{V}\end{bmatrix}, \tag{45}$$

where the indices $U$, $V$ and $W$ refer to the spatial directions $x$, $y$ and $z$ respectively. Each entry $C_{PQ}(M,N)$ of matrix $\mathbf{C}$ is determined by applying a unit point load $F_Q^N$ in direction $Q \in \{U,V,W\}$ at node $N$ and, using equation (44), computing the Fourier series expansion of the resulting displacement in direction $P \in \{U,V,W\}$ at node $M$, from the series expansion of the surface stress $\sigma_Q^N(x,y,H)$ associated with the applied load, i.e.

$$\sigma_Q^N(x,y,H) = \begin{cases}\frac{F_Q^N}{a_x a_y}, & \text{if}\begin{cases} x^N-\frac{a_x}{2} \le x \le x^N+\frac{a_x}{2}\\ y^N-\frac{a_y}{2} \le y \le y^N+\frac{a_y}{2}\end{cases}\\ 0, & \text{otherwise.}\end{cases} \tag{46}$$

The generic surface stress distribution given by (46) corresponds to a two-dimensional periodic rectangle function of widths $a_x$ and $a_y$, and spatial periods $L_x$ and $L_y$, in directions $x$ and $y$ respectively.

Entries of the compliance matrix corresponding to two pairs of nodes ($M_1$,$N_1$) and ($M_2$,$N_2$) are equal if $M_1$ and $M_2$ are in the same relative position with respect to $N_1$ and $N_2$, respectively. Similar considerations apply (with attention to signs) when the two pairs of nodes are symmetrical with respect to the vertical plane containing the direction of motion, which is also a plane of material symmetry. Hence in practice, taking advantage of configurational similarities and symmetry, as described in further detail by Zéhil and Gavin (2013b), unit point loads need only be applied at one extremity of the leading edge, and the trailing edge, of the candidate contact surface.

## 5. Three-dimensional transversely isotropic formulation

It is here assumed that the properties of the layer are symmetric about the $z$-axis only. The layer is hence transversely isotropic in the $xy$-plane. Following similar steps as the ones described in section 4, equations (30)-(35) are re-written as

$$\sigma_{xx_{mn}} = C_{11_m}^* i\nu_x u_{mn} + C_{12_m}^* i\nu_y v_{mn} + C_{13_m}^* \dot{w}_{mn}, \tag{47}$$

$$\sigma_{yy_{mn}} = C^*_{12_m} i\nu_x u_{mn} + C^*_{11_m} i\nu_y v_{mn} + C^*_{13_m} \dot{w}_{mn}, \tag{48}$$

$$\sigma_{zz_{mn}} = C^*_{13_m} i\nu_x u_{mn} + C^*_{13_m} i\nu_y v_{mn} + C^*_{33_m} \dot{w}_{mn}, \tag{49}$$

$$\tau_{xy_{mn}} = \left(C^*_{11_m} - C^*_{12_m}\right)\left(i\nu_y u_{mn} + i\nu_x v_{mn}\right)/2, \tag{50}$$

$$\tau_{xz_{mn}} = C^*_{44_m}\left(i\nu_x w_{mn} + \dot{u}_{mn}\right), \tag{51}$$

$$\tau_{yz_{mn}} = C^*_{44_m}\left(i\nu_y w_{mn} + \dot{v}_{mn}\right), \tag{52}$$

where $C^*_{ij_m} = C^*_{ij}(\omega_m)$ are given in expression (11). Eliminating non-state variables from equations (27)-(29) and (47)-(52), yields a similar expression of matrix $\mathbf{A}_{mn}$ as in (38), where the shorthand parameters in (39)-(42) become

$$\beta^*_x = \frac{E^*_{T_m}}{1-\nu^{*2}_{T_m}}\nu_x^2 + \frac{E^*_{T_m}}{2\left(1+\nu^*_{T_m}\right)}\nu_y^2 - \rho V_s^2\nu_x^2, \tag{53}$$

$$\beta^*_y = \frac{E^*_{T_m}}{1-\nu^{*2}_{T_m}}\nu_y^2 + \frac{E^*_{T_m}}{2\left(1+\nu^*_{T_m}\right)}\nu_x^2 - \rho V_s^2\nu_x^2, \tag{54}$$

$$\beta^*_{xy} = \frac{E^*_{T_m}\nu_x\nu_y}{2\left(1-\nu^*_{T_m}\right)}, \quad G^*_m = G^*_{LT_m}, \tag{55}$$

$$\zeta^* = \frac{1-\nu^*_{T_m} - 2\nu^*_{TL_m}\nu^*_{LT_m}}{E^*_{L_m}\left(1-\nu^*_{T_m}\right)} \quad \text{and} \quad \xi^* = \frac{E^*_{T_m}}{E^*_{L_m}}\frac{\nu^*_{LT_m}}{1-\nu^*_{T_m}}. \tag{56}$$

## 6. Three-dimensional orthotropic formulation

Generalizing further, we consider here an orthogonally anisotropic layer. The principal directions of orthotropy are designated by the numbers 1, 2 and 3, with the 3-axis oriented in the vertical direction $z$. A spatially periodic load, in directions $x$ and $y$, is applied to the upper boundary of the layer, as depicted in figure 2. The load moves at a constant speed $V_s$ in direction $x$, which is at an angle $\theta$ from the 1-axis, in the horizontal plane.

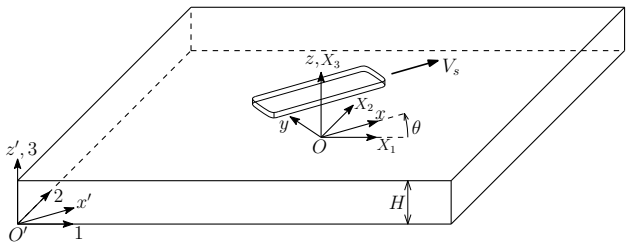


Figure 2: Spatially periodic load moving at constant speed $V_s$, in direction $x$, on the upper boundary of an orthotropic layer. Directions 1, 2 and 3 correspond to the principal directions of orthotropy.

The constitutive relation in (25), whose matrix of elastic moduli $\mathbf{C}^*_m = \mathbf{C}^*(\omega_m)$ in coordinate system $OX_1X_2X_3$ is given by (9), can be expressed in coordinate system $Oxyz$. The transformed matrix of elastic moduli $\bar{\mathbf{C}}^*_m$ is of the form

$$\bar{\mathbf{C}}^*(\omega_m) = \begin{bmatrix} \bar{C}^*_{11_m} & \bar{C}^*_{12_m} & \bar{C}^*_{13_m} & 0 & 0 & \bar{C}^*_{16_m} \\ \bar{C}^*_{12_m} & \bar{C}^*_{22_m} & \bar{C}^*_{23_m} & 0 & 0 & \bar{C}^*_{26_m} \\ \bar{C}^*_{13_m} & \bar{C}^*_{23_m} & \bar{C}^*_{33_m} & 0 & 0 & \bar{C}^*_{36_m} \\ 0 & 0 & 0 & \bar{C}^*_{44_m} & \bar{C}^*_{45_m} & 0 \\ 0 & 0 & 0 & \bar{C}^*_{45_m} & \bar{C}^*_{55_m} & 0 \\ \bar{C}^*_{16_m} & \bar{C}^*_{26_m} & \bar{C}^*_{36_m} & 0 & 0 & \bar{C}^*_{66_m} \end{bmatrix}. \tag{57}$$

Detailed expressions of the transformed moduli $\bar{C}^*_{ij_m}$, in terms of the principal elastic moduli $C^*_{ij_m}$ and the angle $\theta$ defining the direction of movement are derived according to fourth order contravariant tensor transformation rules

(e.g. Fung and Tong, 2001). These expressions are given below

$$\bar{C}^*_{11_m} = C^*_{11_m} + \left(C^*_{11_m} + C^*_{22_m} - 2C^*_{12_m} - 4C^*_{66_m}\right)\sin^4(\theta) + 2\left(C^*_{12_m} - C^*_{11_m} + 2C^*_{66_m}\right)\sin^2(\theta), \tag{58}$$

$$\bar{C}^*_{22_m} = C^*_{22_m} + \left(C^*_{11_m} + C^*_{22_m} - 2C^*_{12_m} - 4C^*_{66_m}\right)\sin^4(\theta) + 2\left(C^*_{12_m} - C^*_{22_m} + 2C^*_{66_m}\right)\sin^2(\theta), \tag{59}$$

$$\bar{C}^*_{33_m} = C^*_{33_m}, \tag{60}$$

$$\bar{C}^*_{44_m} = C^*_{44_m}\cos^2(\theta) + C^*_{55_m}\sin^2(\theta), \tag{61}$$

$$\bar{C}^*_{55_m} = C^*_{55_m}\cos^2(\theta) + C^*_{44_m}\sin^2(\theta), \tag{62}$$

$$\bar{C}^*_{66_m} = C^*_{66_m} + \left(C^*_{11_m} + C^*_{22_m} - 2C^*_{12_m} - 4C^*_{66_m}\right)\sin^2(2\theta)/4, \tag{63}$$

$$\bar{C}^*_{12_m} = C^*_{12_m} + \left(C^*_{11_m} + C^*_{22_m} - 2C^*_{12_m} - 4C^*_{66_m}\right)\sin^2(2\theta)/4, \tag{64}$$

$$\bar{C}^*_{13_m} = C^*_{13_m}\cos^2(\theta) + C^*_{23_m}\sin^2(\theta), \tag{65}$$

$$\bar{C}^*_{23_m} = C^*_{23_m}\cos^2(\theta) + C^*_{13_m}\sin^2(\theta), \tag{66}$$

$$\bar{C}^*_{16_m} = \left(C^*_{22_m} - C^*_{11_m}\right)\sin(2\theta)/4 - \left(C^*_{11_m} + C^*_{22_m} - 2C^*_{12_m} - 4C^*_{66_m}\right)\sin(4\theta)/8, \tag{67}$$

$$\bar{C}^*_{26_m} = \left(C^*_{22_m} - C^*_{11_m}\right)\sin(2\theta)/4 + \left(C^*_{11_m} + C^*_{22_m} - 2C^*_{12_m} - 4C^*_{66_m}\right)\sin(4\theta)/8, \tag{68}$$

$$\bar{C}^*_{36_m} = \left(C^*_{23_m} - C^*_{13_m}\right)\sin(2\theta)/2, \tag{69}$$

$$\bar{C}^*_{45_m} = \left(C^*_{44_m} - C^*_{55_m}\right)\sin(2\theta)/2. \tag{70}$$

Following an approach similar to that described in section 5, equations (47)-(52) are re-derived in the form

$$\sigma_{xx_{mn}} = i\left(\bar{C}^*_{11_m}\nu_x + \bar{C}^*_{16_m}\nu_y\right)u_{mn} + i\left(\bar{C}^*_{12_m}\nu_y + \bar{C}^*_{16_m}\nu_x\right)v_{mn} + \bar{C}^*_{13_m}\dot{w}_{mn}, \tag{71}$$

$$\sigma_{yy_{mn}} = i\left(\bar{C}^*_{12_m}\nu_x + \bar{C}^*_{26_m}\nu_y\right)u_{mn} + i\left(\bar{C}^*_{22_m}\nu_y + \bar{C}^*_{26_m}\nu_x\right)v_{mn} + \bar{C}^*_{23_m}\dot{w}_{mn}, \tag{72}$$

$$\sigma_{zz_{mn}} = i\left(\bar{C}^*_{13_m}\nu_x + \bar{C}^*_{36_m}\nu_y\right)u_{mn} + i\left(\bar{C}^*_{23_m}\nu_y + \bar{C}^*_{36_m}\nu_x\right)v_{mn} + \bar{C}^*_{33_m}\dot{w}_{mn}, \tag{73}$$

$$\tau_{xy_{mn}} = i\left(\bar{C}^*_{16_m}\nu_x + \bar{C}^*_{66_m}\nu_y\right)u_{mn} + i\left(\bar{C}^*_{26_m}\nu_y + \bar{C}^*_{66_m}\nu_x\right)v_{mn} + \bar{C}^*_{36_m}\dot{w}_{mn}, \tag{74}$$

$$\tau_{xz_{mn}} = \bar{C}^*_{55_m}\dot{u}_{mn} + \bar{C}^*_{45_m}\dot{v}_{mn} + i\left(\bar{C}^*_{45_m}\nu_y + \bar{C}^*_{55_m}\nu_x\right)w_{mn}, \tag{75}$$

$$\tau_{yz_{mn}} = \bar{C}^*_{45_m}\dot{u}_{mn} + \bar{C}^*_{44_m}\dot{v}_{mn} + i\left(\bar{C}^*_{44_m}\nu_y + \bar{C}^*_{45_m}\nu_x\right)w_{mn}. \tag{76}$$

Referring back to system (37), eliminating non-state variables from equations (27)-(29) and (71)-(76) results in the following expression of the state matrix $\mathbf{A}_{mn}$

$$\mathbf{A}_{mn} = \begin{bmatrix} 0 & -i\xi^*_x & -i\xi^*_y & \zeta^* & 0 & 0 \\ -i\nu_x & 0 & 0 & 0 & \Gamma^*_1 & \Gamma^*_3 \\ -i\nu_y & 0 & 0 & 0 & \Gamma^*_3 & \Gamma^*_2 \\ -\rho V_s^2\nu_x^2 & 0 & 0 & 0 & -i\nu_x & -i\nu_y \\ 0 & \beta^*_x & \beta^*_{xy} & -i\xi^*_x & 0 & 0 \\ 0 & \beta^*_{xy} & \beta^*_y & -i\xi^*_y & 0 & 0 \end{bmatrix}. \tag{77}$$

Shorthand parameters appearing in (38) are defined below

$$\Gamma^*_1 = \frac{\bar{C}^*_{44_m}}{\bar{C}^*_{44_m}\bar{C}^*_{55_m} - \bar{C}^{*2}_{45_m}} \;\; ; \;\; \Gamma^*_2 = \frac{\bar{C}^*_{55_m}}{\bar{C}^*_{44_m}\bar{C}^*_{55_m} - \bar{C}^{*2}_{45_m}} \;\; ; \Gamma^*_3 = -\frac{\bar{C}^*_{45_m}}{\bar{C}^*_{44_m}\bar{C}^*_{55_m} - \bar{C}^{*2}_{45_m}}, \tag{78}$$

$$\beta^*_x = \left(\bar{C}^*_{11_m} - \frac{\bar{C}^{*2}_{13_m}}{\bar{C}^*_{33_m}}\right)\nu_x^2 + \left(\bar{C}^*_{66_m} - \frac{\bar{C}^{*2}_{36_m}}{\bar{C}^*_{33_m}}\right)\nu_y^2 + 2\left(\bar{C}^*_{16_m} - \frac{\bar{C}^*_{13_m}\bar{C}^*_{36_m}}{\bar{C}^*_{33_m}}\right)\nu_x\nu_y - \rho V_s^2\nu_x^2, \tag{79}$$

$$\beta^*_y = \left(\bar{C}^*_{66_m} - \frac{\bar{C}^{*2}_{36_m}}{\bar{C}^*_{33_m}}\right)\nu_x^2 + \left(\bar{C}^*_{22_m} - \frac{\bar{C}^{*2}_{23_m}}{\bar{C}^*_{33_m}}\right)\nu_y^2 + 2\left(\bar{C}^*_{26_m} - \frac{\bar{C}^*_{23_m}\bar{C}^*_{36_m}}{\bar{C}^*_{33_m}}\right)\nu_x\nu_y - \rho V_s^2\nu_x^2, \tag{80}$$

$$\beta_{xy}^{*} = \left( \bar{C}_{16_m}^{*} - \frac{\bar{C}_{13_m}^{*} \bar{C}_{36_m}^{*}}{\bar{C}_{33_m}^{*}} \right) \nu_x^2 + \left( \bar{C}_{26_m}^{*} - \frac{\bar{C}_{23_m}^{*} \bar{C}_{36_m}^{*}}{\bar{C}_{33_m}^{*}} \right) \nu_y^2 + \left( \bar{C}_{12_m}^{*} + \bar{C}_{66_m}^{*} - \frac{\bar{C}^{*2}_{36_m} + \bar{C}_{13_m}^{*} \bar{C}_{23_m}^{*}}{\bar{C}_{33_m}^{*}} \right) \nu_x \nu_y, \tag{81}$$

$$\xi_x^{*} = \frac{\bar{C}_{13_m}^{*} \nu_x + \bar{C}_{36_m}^{*} \nu_y}{\bar{C}_{33_m}^{*}} \quad ; \quad \xi_y^{*} = \frac{\bar{C}_{36_m}^{*} \nu_x + \bar{C}_{23_m}^{*} \nu_y}{\bar{C}_{33_m}^{*}} \quad \text{and} \quad \zeta^{*} = \bar{C}^{*-1}_{33_m}. \tag{82}$$

In the case of an orthotropic layer, the vertical plane containing the direction of motion is generally not a plane of material symmetry, as opposed to the case of isotropic and transversely isotopic layers. Consequently, when forming the compliance matrix of an orthotropic layer, unit point loads must be applied at both extremities of the leading edge, and the trailing edge, of the candidate contact surface.

## 7. Isotropic formulation in plain strain

A two-dimensional boundary-element formulation for the layer in plane strain can be deduced from the three-dimensional formulation presented in section 4, by eliminating all dependences on the spatial variable $y$, which corresponds to dropping the subscript $n$, and by setting out-of-plane deformation and strain coefficients to zero, i.e.

$$v_m = 0, \qquad \epsilon_{yy_m} = 0, \qquad \gamma_{xy_m} = 0, \quad \text{and} \quad \gamma_{yz_m} = 0. \tag{83}$$

The behavioral law in (26) hence implies

$$\tau_{xy_m} = 0, \qquad \tau_{yz_m} = 0, \quad \text{and} \quad \sigma_{yy_m} = \lambda_m^{*} \left( \epsilon_{xx_m} + \epsilon_{zz_m} \right). \tag{84}$$

In light of (83) and (84), equilibrium equations (27)-(29) specialize into

$$-\rho V_s^2 \nu_x^2 u_m = i\nu_x \sigma_{xx_m} + \dot{\tau}_{xz_m}, \tag{85}$$

$$-\rho V_s^2 \nu_x^2 w_m = i\nu_x \tau_{xz_m} + \dot{\sigma}_{zz_m}, \tag{86}$$

Constitutive equations (30)-(35) also reduce to three relevant expressions, i.e.

$$\sigma_{xx_m} = \frac{E_m^{*}}{(1+\nu_m^{*})(1-2\nu_m^{*})} \left[ (1-\nu_m^{*}) \, i\nu_x u_m + \nu_m^{*} \dot{w}_m \right], \tag{87}$$

$$\sigma_{zz_m} = \frac{E_m^{*}}{(1+\nu_m^{*})(1-2\nu_m^{*})} \left[ (1-\nu_m^{*}) \, \dot{w}_m + \nu_m^{*} i\nu_x u_m \right], \tag{88}$$

$$\tau_{xz_m} = \sigma_{xz_m} = \frac{E_m^{*}}{2(1+\nu_m^{*})} \left( i\nu_x w_{mn} + \dot{u}_{mn} \right). \tag{89}$$

The complex-valued state vector $\mathbf{q}_{mn}(z)$ defined in (36) becomes

$$\mathbf{q}_m(z) = \left\langle w_m(z), u_m(z), \sigma_{zz_m}(z), \tau_{xz_m}(z) \right\rangle^T. \tag{90}$$

Eliminating the remaining quantities from equations (85)-(89) results in a reduced and specialized version of equation (37), i.e.

$$\dot{\mathbf{q}}_m(z) = \mathbf{A}_m \mathbf{q}_m(z) \tag{91}$$

where $\mathbf{A}_{mn}$ is a complex-valued $4 \times 4$ matrix given by

$$\mathbf{A}_m = \begin{bmatrix} 0 & -i\xi^{*}\nu_x & \zeta^{*} & 0 \\ -i\nu_x & 0 & 0 & G_m^{*-1} \\ -\rho V_s^2 \nu_x^2 & 0 & 0 & -i\nu_x \\ 0 & \beta^{*} & -i\xi^{*}\nu_x & 0 \end{bmatrix}, \tag{92}$$

with $\zeta^{*}$ and $\xi^{*}$ given by (42), and a new shorthand parameter $\beta^{*}$ defined as

$$\beta^{*} = \left( \frac{E_m^{*}}{1-\nu_m^{*2}} - \rho V_s^2 \right) \nu_x^2. \tag{93}$$

## 8. Transversely isotropic formulation in plain strain

A transversely isotropic formulation in plain strain can also be deduced from its three-dimensional counterpart derived in section 5. Following a similar approach to that presented in section 7, all dependences on the spatial variable $y$ are eliminated by dropping the subscript $n$; the out-of-plane deformation and strain coefficients are set to zero, according to expression (83), which also yields equations (85)-(86). The constitutive equations in (47)-(52) reduce to the three relevant expressions below

$$\sigma_{xx_m} = C^*_{11_m} i\nu_x u_m + C^*_{13_m} \dot{w}_m, \tag{94}$$

$$\sigma_{zz_m} = C^*_{13_m} i\nu_x u_m + C^*_{33_m} \dot{w}_m, \tag{95}$$

$$\tau_{xz_m} = C^*_{44_m} \left(i\nu_x w_m + \dot{u}_m\right). \tag{96}$$

Defining the state vector as in (90), then combining equations (85)-(86) and (94)-(96), while eliminating all non-state variables, produces a similar formulation as in (92), where $\zeta^*$ and $\xi^*$ are given by (56), $G^*_{LT_m}$ replaces $G^*_m$, and $\beta^*$ is redefined as

$$\beta^* = \left(\frac{E^*_{T_m}}{1 - {\nu^*_{T_m}}^2} - \rho V_s^2\right)\nu_x^2. \tag{97}$$

## 9. Consistency checks

### *9.1. Linking the compressible and incompressible isotropic formulations*

The full 3D *compressible* formulation derived in section 4 is checked against the *incompressible* formulation presented by Zéhil and Gavin (2013b). Setting Poisson's ratio $\nu^*(\omega)$ to the real and constant value of 1/2, the shorthand parameters defined in (39)-(42) become

$$\beta^*_x = G^*_m \left(4\nu_x^2 + \nu_y^2\right) - \rho V_s^2 \nu_x^2, \tag{98}$$

$$\beta^*_y = G^*_m \left(4\nu_y^2 + \nu_x^2\right) - \rho V_s^2 \nu_x^2, \tag{99}$$

$$\beta^*_{xy} = 3G^*_m \nu_x \nu_y, \tag{100}$$

$$\zeta^* = 0 \quad \text{and} \quad \xi^* = 1. \tag{101}$$

Substituting equations (98)-(101) into (38) and comparing to expressions (27) and (45) of Zéhil and Gavin (2013b) reveals that the the two formulations match analytically for $\nu^*(\omega) = 1/2$. Consequently, the incompressible formulations proposed by Qiu (2006) and Zéhil and Gavin (2013b) may be regarded as particular cases of the more general formulations presented in sections 4 and 7 of this work.

### *9.2. Linking the compressible orthotropic, transversely isotropic and isotropic formulations*

It can be easily verified that the orthotropic formulation given by equations (9) and (77)-(82) matches the transversely isotropic formulation in equations (11), (38) and (53)-(56) when $E^*_1 = E^*_2 = E^*_T$, $\nu^*_{31} = \nu^*_{32} = \nu^*_{LT}$, $G^*_{13} = G^*_{23} = G^*_{LT}$, and $G^*_{12} = E^*_T / \left(2\left(1 + \nu^*_T\right)\right)$. It is noteworthy that, in this case, all combinations of $C^*_{ij_m}$ terms enclosed within parenthesis in equations (58)-(70) and multiplying functions of the variable $\theta$ vanish. Hence as expected, the polar anisotropic formulation is rendered independent of the direction of motion.

The parameters defined by expressions (53)-(56) also match those defined in equations (39)-(42) when $\nu^*_{LT_m} = \nu^*_{T_m} = \nu^*_m$, $E^*_{L_m} = E^*_{T_m} = E^*_m$ and $G^*_{LT_m} = E^*_m / \left(2\left(1 + \nu^*_m\right)\right) = G^*_m$. The transversely isotropic formulation specializes into the isotropic formulations in this case.

| a | Truncation order $N_t$ [Number of Terms] | | | | | |
|---|---|---|---|---|---|---|
| [mm] | 100 | 200 | 500 | 750 | 1000 | 1500 |
| 1.00 | 1.2406 | 1.1777 | 1.2025 | 1.2024 | 1.1992 | 1.2012 |
| 0.75 | N/A | 1.2867 | 1.2837 | 1.2856 | 1.2846 | 1.2849 |
| 0.50 | N/A | 1.2882 | 1.2906 | 1.2896 | 1.2900 | 1.2900 |
| 0.30 | N/A | N/A | 1.2906 | 1.2894 | 1.2905 | 1.2910 |
| 0.25 | N/A | N/A | 1.2914 | 1.2910 | 1.2911 | 1.2912 |
| 0.20 | N/A | N/A | 1.2925 | 1.2923 | 1.2920 | 1.2923 |
| 0.15 | N/A | N/A | N/A | 1.2927 | 1.2930 | 1.2931 |

Table 1: Effects of nodal spacing and truncation order on the convergence of 3D models.

## 10. Application examples to rolling resistance

In the following numerical examples, we consider a viscoelastic layer of thickness $H = 1$ mm and density $\rho = 1000$ kg/m$^3$. For simplicity, and without prejudice to the generality of the proposed formulations, which can accommodate any relaxation spectrum to each of the model's parameters, it is further assumed that Poisson's ratios are constant and that any frequency-dependent dynamic (longitudinal or shear) modulus $\mathcal{P}(\omega)$ follows the standard linear solid model defined by the following master-curves

$$\begin{aligned} \mathcal{P}'(\omega) &= \mathcal{P}_0(1+f_{\mathcal{P}})\frac{(1+f_{\mathcal{P}})+\omega^2\tau_{\mathcal{P}}^2}{(1+f_{\mathcal{P}})^2+\omega^2\tau_{\mathcal{P}}^2}, \\ \mathcal{P}''(\omega) &= \mathcal{P}_0(1+f_{\mathcal{P}})\frac{f_{\mathcal{P}}\omega\tau}{(1+f_{\mathcal{P}})^2+\omega^2\tau_{\mathcal{P}}^2}, \end{aligned} \tag{102}$$

where $\mathcal{P}_0 = \mathcal{P}'(0)$ is the static modulus, $\tau_{\mathcal{P}}$ s is the creep time and $f_{\mathcal{P}} = \mathcal{P}'(0)/\mathcal{P}'(\infty) - 1 = 1$. The viscoelastic resistances incurred by a rigid cylinder and a rigid sphere rolling in steady-state on the layer are sought, in two and three-dimensional settings respectively.

In the two-dimensional setting, we consider a rigid cylinder of radius $R = 2$ cm rolling on the layer at a constant speed $V_s$ while subjected to a vertical load per unit length $P$. A constant coefficient of surface friction $\mu = 0.2$ is retained between the rolling cylinder and the layer's upper boundary. The cylinder is driven by a constant force per unit length $Q_x$, applied tangentially to its upper generatrix in the direction of motion, i.e. towards the positive side of the $x$-axis. The described setting is taken to be spatially periodic, of period $L_x = 0.2$ m, in direction $x$.

The three-dimensional setting corresponds to that of a hard sphere of radius $R = 2$ cm, subjected to a vertical load $P$, and rolled on the layer by a driving force $Q_x$ applied at its center, in the direction of positive $x$. Spatial periodicity is assumed in directions $x$ and $y$ with spatial periods $L_x = L_y = 0.2$ m. Given that the contribution of surface friction to rolling resistance is marginal (e.g. Greenwood and Tabor, 1958; Qiu, 2006; Tabor, 1955; Zéhil and Gavin, 2013b), $\mu$ is set to zero to reduce three-dimensional computational costs.

In each of the following examples, the candidate contact surface on the layer's upper boundary is discretized into nodes and a compliance matrix $\mathbf{C}$ is built based on the formulations outlined in sections 4 through 8. Rolling resistance is then evaluated based on the solution to the rolling contact problem between: (i) the layer's upper boundary, which is fully characterized by $\mathbf{C}$, and (ii) the rigid rolling object. Almost any contact solving strategy may be used to this aim. The contact algorithms described in Zéhil and Gavin (2013a) were retained for this work.

To optimize further the computational costs related to the three-dimensional models, appropriate nodal spacings and truncation orders are sought such to yield a satisfactory level of convergence. To this aim, rolling resistance is evaluated, in the conditions of section 10.3, using a nodal spacing $a = a_x = a_y$ varying from 0.15 mm to 1 mm and a truncation order $N_t = N_{t_x} = N_{t_y}$ ranging from 100 to 1500 terms. The resulting values are reproduced in table 1 and found to fall within 9% of each other. It is furthermore noted that, when the spacing between nodes is less than or equal to 0.75 mm, the results are well within 0.75%, which is suitable for most engineering applications. Table 1 furthermore reveals that the truncation order has less impact on the accuracy of the solution than the nodal spacing. However, when the spatial mesh is refined, the surface stress distribution given by the generic expression in (46) takes a larger 'bandwidth.' Consequently, the number of terms in the Fourier series must be increased to prevent oscillations in the compliance matrix that would otherwise render the rolling contact problem impossible to solve ("N/A" entries in

table 1). Based on these observations, a nodal spacing of $a_x = a_y = 0.50$ mm and a truncation order of $N_{t_x} = N_{t_y} = 200$ terms are retained for the purposes of the following examples.

### *10.1. Compressible isotropic layer in 2D and 3D*

#### *10.1.1. Rolling cylinder in 2D*

In this first two-dimensional example, the viscoelastic layer is taken to be compressible and isotropic with a static Young modulus $E_0 = 9$ MPa and a creep time $\tau_{E_0} = 0.25$ s. A linear speed $V_s = 5$ cm/s is retained for the rolling cylinder subjected to a vertical load $P = 5$ kN/m. The frequency-independent parameter $\nu$ of the layer is varied between $-1$ and 0.5 to illustrate the incidence of Poisson's ratio on the dynamic indentation and the rolling resistance.

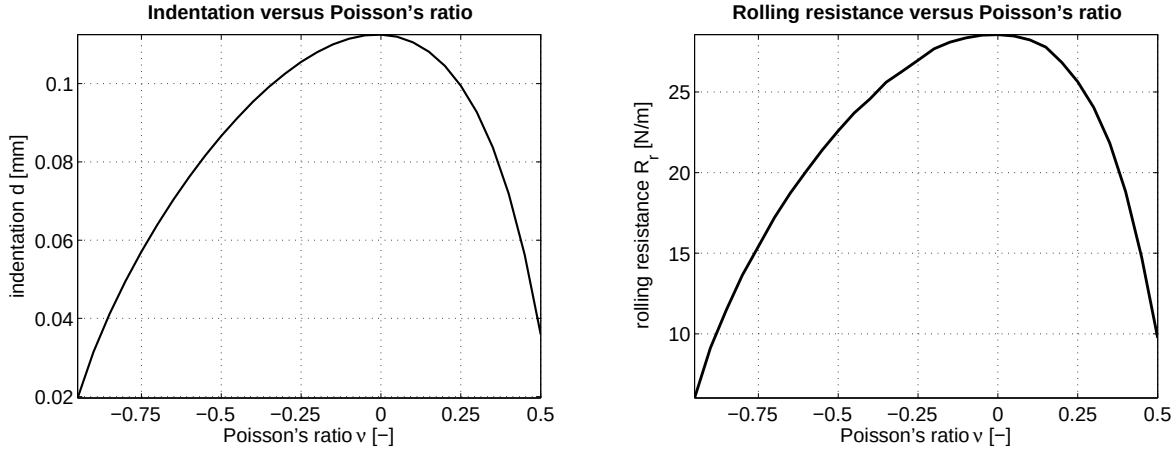


(a) $d$ versus $\nu$ (b) $R_r$ versus $\nu$

Figure 3: Rigid cylinder on a compressible isotropic viscoelastic layer (2D model in plane strain): variations of indentation and rolling resistance with Poisson's ratio.

The cylinder's penetration into the viscoelastic layer and the rolling resistance it is subjected to, including a marginal contribution from surface friction, are plotted in figures 3(a) and 3(b) respectively, against Poisson's ratio. It is noteworthy that the relationship between indentation and rolling resistance is roughly linear in this case.

#### *10.1.2. Rolling sphere in 3D*

The compressible isotropic viscoelastic layer described in section 10.1.1 is now modeled in three-dimensions. The sphere is rolled on the layer at the same speed as the cylinder, i.e. at $V_s = 5$ cm/s, while subjected to a vertical load $P = 100$ N. The average contact pressure corresponding to $P$ is roughly the same as for the cylinder in section 10.1.1.

The sphere's penetration into the viscoelastic layer and the rolling resistance it is subjected to are plotted in figures 4(a) and 4(b) respectively, against Poisson's ratio. The corresponding curves are qualitatively similar to the curves shown in figure 3 for the cylinder. Both quantities are maximized by a Poisson ratio that is close to zero, as predicted by the approximate equations reproduced in (1)-(3) for spheres. As noted in section 10.1.1 for cylinders, the dependence of rolling resistance on the sphere's penetration into the layer, for the current range of parameters, appears to be linear.

### *10.2. Transversely isotropic layer in 2D*

The rolling of a hard cylinder on a transversely isotropic viscoelastic layer is considered here and analyzed in plane strain. The material model is further characterized by the following values of its parameters: $E_{L_0} = 4$ MPa, $E_{T_0} = 9$ MPa, $G_{LT_0} = 3$ MPa, $\nu_T = 0.45$ and $\nu_{LT} = 0$. All creep times are taken equal to 0.25 s.

The penetration of the rolling cylinder into the layer and the rolling resistance it incurs are plotted in figures 5(a) and 5(b) respectively, against the rolling speed $V_s$ ranging from 0.1 cm/s to 50 cm/s. Starting at 500 N, the applied load $P$ is increased by steps of 500 N, up to 5 kN. The shapes of the curves are typical of viscoelastic models: the indentation decreases with increasing speed between two asymptotes, as the layer's stiffness does; alternatively,

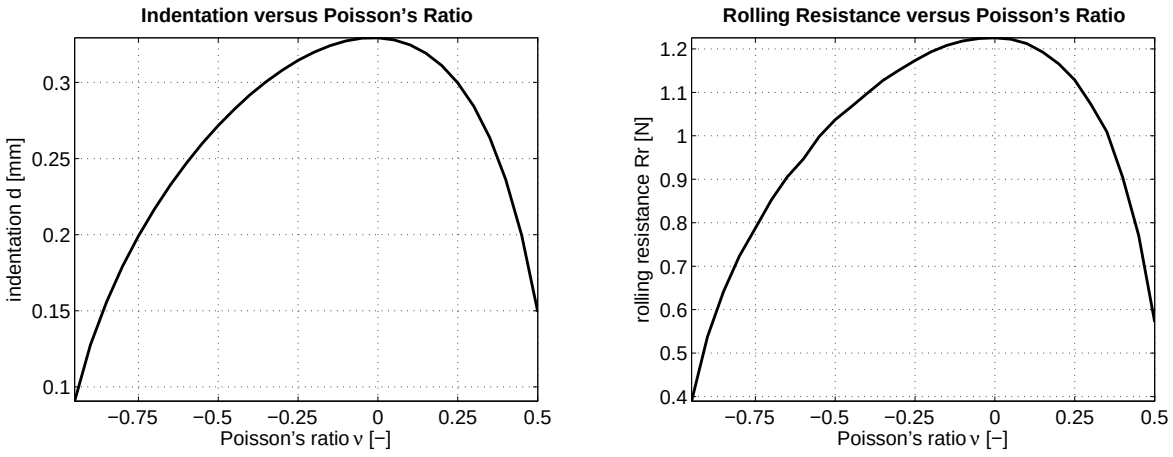


(a) $d$ versus $\nu$ (b) $R_r$ versus $\nu$

Figure 4: Rigid sphere on a compressible isotropic viscoelastic layer (3D model): variations of indentation and rolling resistance with Poisson's ratio.

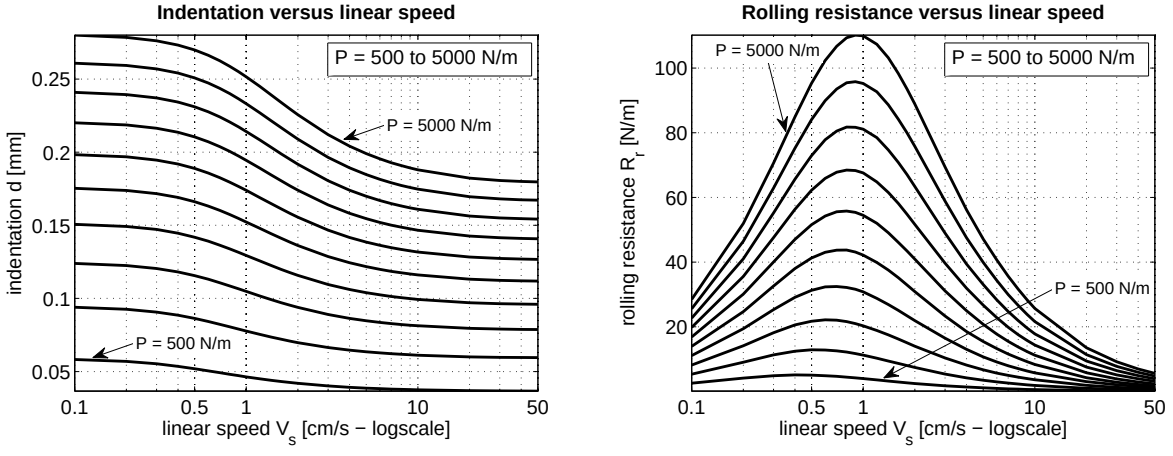


(a) $d$ versus $V_s$ (b) $R_r$ versus $V_s$

Figure 5: Rigid cylinder on a transversely isotropic viscoelastic layer (2D model in plane strain): variations of indentation and rolling resistance with rolling speed. The curves correspond to different load levels between 500 N and 5 kN, in steps of 500 N. Indentation and rolling resistance increase with the applied load.

| Index $i$ | 1 | 2 | 3 |
|---|---|---|---|
| $E_{i_0}$ [MPa] | 9.00 | 6.00 | 4.00 |
| $\tau_{E_i}$ [s] | 2.00 | 0.05 | 0.25 |
| Indices $i$ / $j$ | 1 / 2 | 1 / 3 | 2 / 3 |
| $G_{ij_0}$ [MPa] | 3.00 | 3.00 | 3.00 |
| $\tau_{G_{ij}}$ [s] | 0.25 | 2.00 | 0.05 |
| $\nu_{ij}$ [-] | 0.20 | 0.00 | 0.50 |

Table 2: Static moduli, creep times and Poisson ratios characterizing the orthotropic viscoelastic layer.

hysteretic dissipations tend to zero as the time to cover a distance equal to a dimension of reference, such as the radius of the rolling object, becomes very small, or very large, as compared to the material's internal time scales. A peak in rolling resistance is hence reached at an intermediate velocity depending on the parameters of the problem, including the relaxation spectrum of the layer.

In figure 6, rolling resistance values from figure 5(b) are plotted against the corresponding indentations taken from figure 5(a), which produces one curve for each value of the load $P$. Referring to Figure 5(a), the end of each curve in Figure 6 with the higher rolling resistance and indentation corresponds to the lower rolling speed of 0.1 cm/s. A roughly quadratic dependence of rolling resistance on indentation is revealed in this case.

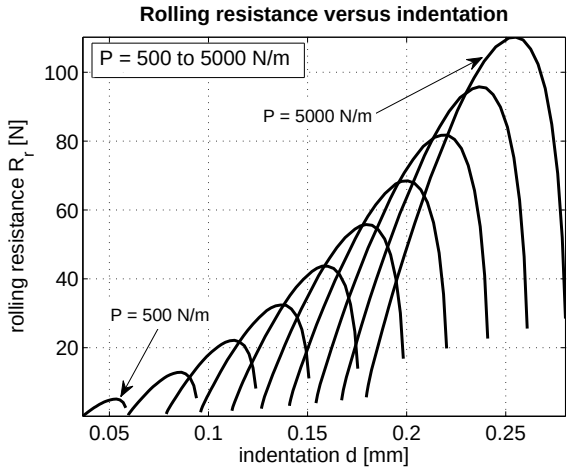


Figure 6: Rigid cylinder on a transversely isotropic viscoelastic layer (2D model in plane strain): variations of rolling resistance with indentation for different values of the applied load. The curves correspond to different load levels between 500 N and 5 kN, in steps of 500 N. Indentation and rolling resistance increase with the applied load.

### *10.3. Orthotropic layer in 3D*

The rolling of a hard sphere on an orthotropic layer is considered in this example. The viscoelastic material model of the layer is further characterized by the static moduli, creep times and frequency-independent Poisson ratios given in table 2.

The $x$-axis, corresponding to the direction of motion, is defined by its angle $\theta$ from the the first axis of orthotropy in the plane of the layer, as depicted in figure 2. The viscoelastic resistance incurred by the rolling sphere is plotted in figure 7(a) against the angle $\theta$, varying between 0 and 90 degrees, for $P = 100$ N and $V_s = 0.1$ and 5 cm/s. Given the choice of parameters in table 2, the dependence of rolling resistance on the direction of motion varies with the rolling speed. For instance, at $V_s = 5$ cm/s, minimum (resp. maximum) rolling resistance occurs when the direction of motion is at an angle of roughly 40 (resp. 90) degrees from the 1-axis. Alternatively, at $V_s = 0.1$ cm/s, maximum and minimum rolling resistances occur when $\theta$ equals 45 and 90 degrees, respectively.

Rolling resistance results as usual from the asymmetry of the normal contact stress distribution, induced by viscoelasticity, in the longitudinal direction. However, in contrast with all previous cases, when the direction of motion is

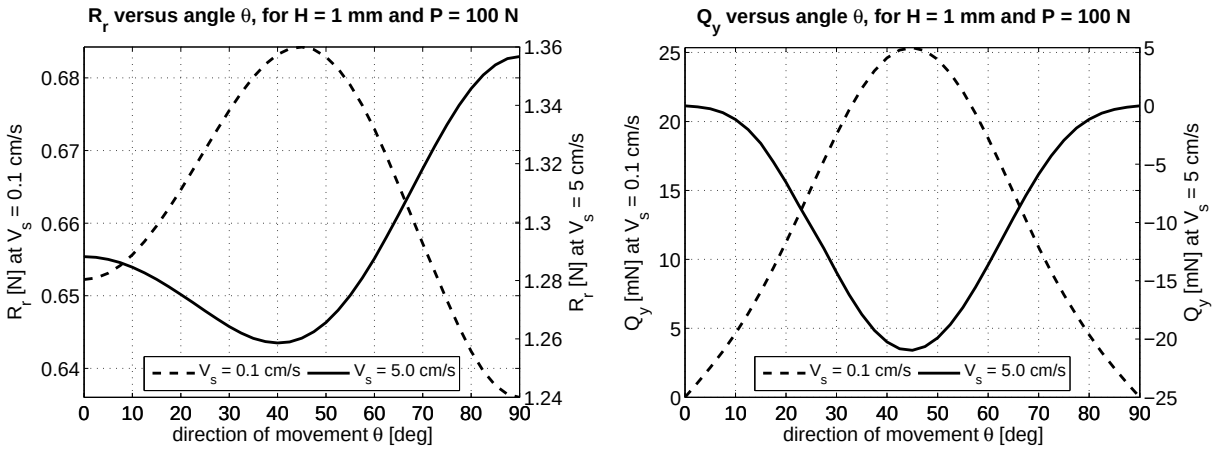


(a) $R_r$ versus $\theta$ (b) $Q_y$ versus $\theta$

Figure 7: Rigid sphere on an orthotropic viscoelastic layer (3D model): variations of rolling resistance and the lateral guiding force with the direction of motion.

at a nonzero angle from the principal axes of orthotropy, the mechanical response of the layer is different on each side of the vertical plane containing the $x$-axis, which results in a lateral asymmetry of contact generating an additional resultant acting on the sphere in direction $y$. Hence, an equal and opposite lateral force $Q_y$ must be applied to the center of the sphere, in addition to $Q_x$, to maintain steady-state motion along a straight path. The variations of $Q_y$ with the direction of motion, for $P = 100$ N and $V_s = 0.1$ and 5 cm/s, are shown in figure 7(b). $Q_y$ reaches a peak at an angle $\theta$ depending on the rate of motion and drops to zero, as expected, along the principal axes of orthotropy. It is interesting to note that the sign of $Q_y$ depends on the rolling speed. For instance, at $V_s = 0.1$ cm/s, the sphere tends to deviate to the right in the absence of lateral support, whereas at $V_s = 5$ cm/s, it tends to deviate to the left.

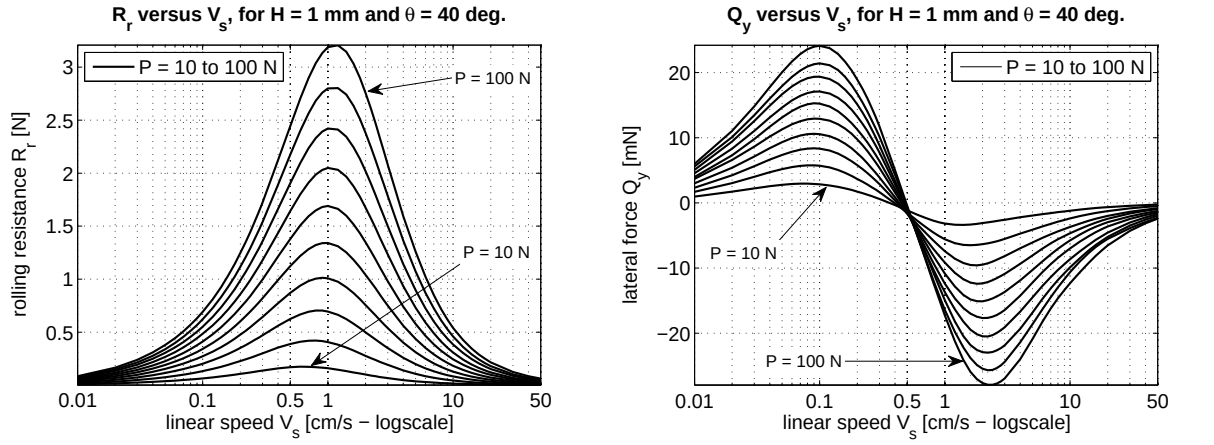


(a) $R_r$ versus $V_s$ (b) $Q_y$ versus $V_s$

Figure 8: Rigid sphere on an orthotropic viscoelastic layer (3D model): variations of rolling resistance and the lateral guiding force with rolling speed. The curves correspond to different load levels between 10 N and 100 N, in steps of 10 N. Rolling resistance and lateral force increase in magnitude with the applied load.

The variations of rolling resistance $R_r$ and of the lateral supporting force $Q_y$ with the rolling speed $V_s$, ranging from 0.01 cm/s to 50 cm/s, are shown in figures 8(a) and 8(b) respectively, for the direction of motion defined by $\theta = 40$ deg. Each curve corresponds to a fixed value of the applied load $P$, which is increased by steps of 10 N,

starting at 10 N and up to a 100 N. The dependence of rolling resistance on the rate of motion is of the usual kind, briefly described for instance in section 10.2. It is again interesting to note that $Q_y$ tends to zero at low and high speeds which confirms its viscoelastic nature. Furthermore, in relation with what was previously noted in figure 7(b) regarding the sign of $Q_y$, figure 8(b) reveals the existence of an intermediate speed at which $Q_y$ also vanishes.

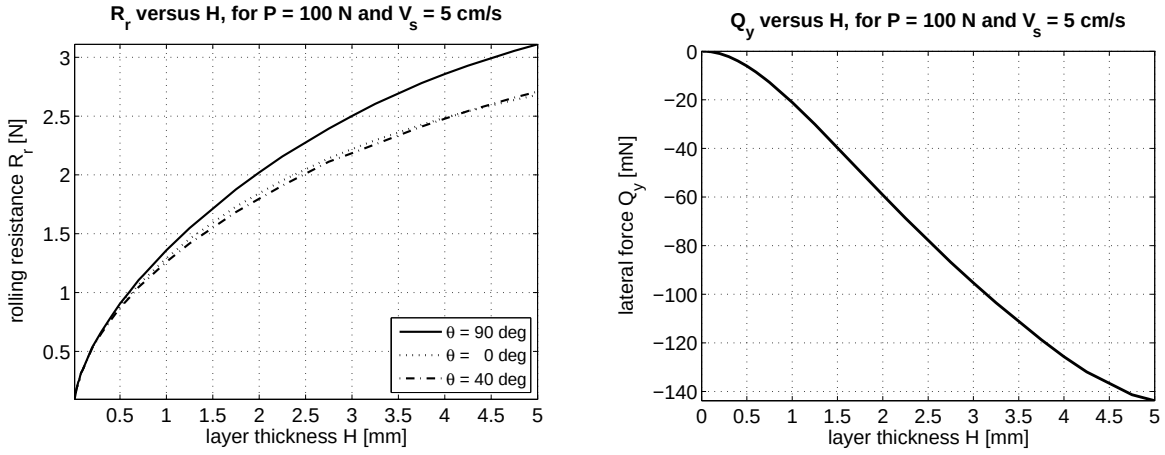


(a) $R_r$ versus $H$ (b) $Q_y$ versus $H$

Figure 9: Rigid sphere on an orthotropic viscoelastic layer (3D model): variations of rolling resistance and the lateral guiding force with the layer's thickness.

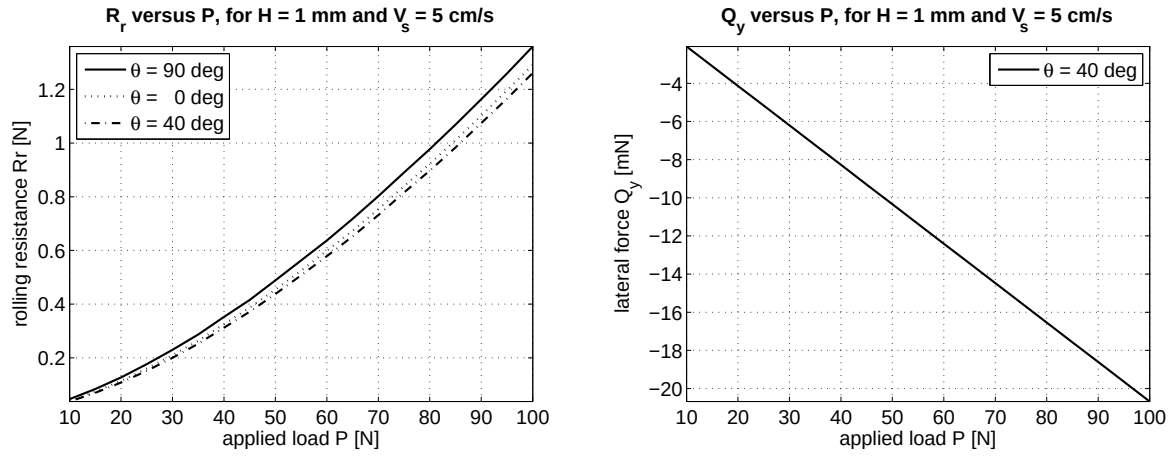


(a) $R_r$ versus $P$ (b) $Q_y$ versus $P$

Figure 10: Rigid sphere on an orthotropic viscoelastic layer (3D model): variations of rolling resistance and the lateral guiding force with the applied load.

The influence of layer thickness ($H$) on the rolling resistance incurred by the sphere ($R_r$) and on the lateral supporting force ($Q_y$) are shown in figures 9(a) and 9(b) respectively, for the directions of motion defined by $\theta = 0$ deg., $\theta = 40$ deg. and $\theta = 90$ deg. The trivial cases corresponding to $Q_y(H, \theta) = 0\ \forall H$ for $\theta = 0$ deg. and $\theta = 90$ deg. are hidden in figure 9(b). As in the case of an incompressible and isotropic foundation (e.g. Qiu, 2006; Zéhil and Gavin, 2013b), the resistance to rolling increases with layer thickness and tends progressively towards a horizontal asymptote corresponding to the limiting case of an orthotropic viscoelastic "half-space". The magnitude of $Q_y$ is also an increasing function of $H$. Its change of curvature is consistent with the existence of a limiting case as $H$ tends to

infinity. The dependence of both quantities ($R_r$ and $Q_y$) on layer thickness can be fitted, for instance, by rational functions with negative poles. These expressions should be further characterized by a numerator that vanishes as $H$ tends to zero and by a denominator of the same degree as the numerator, such that the fitted function tends asymptotically to the "half-space" solution as $H$ becomes large.

Rolling resistance ($R_r$) and lateral force ($Q_y$) are plotted in figures 10(a) and 10(b) respectively, against the applied load $P$, ranging from 10 to 100 N, for $H = 1$ mm, $V_s = 5$ cm/s and for the directions of motion corresponding to $\theta = 0$ deg., $\theta = 40$ deg. and $\theta = 90$ deg. The trivial cases given by $Q_y(P, \theta) = 0 \; \forall P$ for $\theta = 0$ deg. and $\theta = 90$ deg. are hidden from figure 10(b). The resistance to motion and the magnitude of the lateral force increase with the vertical load supported by the rolling sphere, which is in agreement with the information displayed in figures 8(a) and 8(b). The dependence of $Q_y$ on $P$ appears to be quasi-linear. Alternatively, the relationship between $R_r$ and $P$ is well fitted by power laws of the form $R_r(P) = a_p P^{b_p}$. The coefficient $b_p$ falls between 0.49 and 0.55 for the curves plotted in figure 10(a). It is furthermore noteworthy that, in accordance with the results shown earlier in figure 7(a), the dashed curve and the dotted curve in figure 9(a) remain below the solid curve corresponding to the direction of maximum dissipation.

## 11. Conclusions

New two-dimensional and three-dimensional boundary element formulations of *compressible* viscoelastic layers of arbitrary thickness were presented in this work, in a moving frame of reference. These formulations were derived in increasing order of complexity for: (i) compressible isotropic layers, (ii) transversely isotropic layers, and (iii) fully orthotropic layers. The proposed modeling techniques include, extend and complement existing 2D (Qiu, 2006) and 3D (Zéhil and Gavin, 2013b) formulations for *incompressible* layers and are hence characterized by similar (and further improved) strengths, such as: (i) the ability to accommodate any orthotropic linear viscoelastic model comprising as many internal time scales as necessary for each of the nine complex frequency-dependent model parameters, (ii) versatility in that the formulations can be used as components in various problem settings such as steady-state rolling or sliding contact problems involving soft or rigid indenters, and other layers, (iii) accuracy compared to other existing approaches relying on the elastic half-space approximation (e.g. Kalker, 1979; Vollebregt, 2012) in propagating viscoelastic surface effects to the layer's continuum, and posing limitations on how thin the layer can be, (iv) computational efficiency resulting from the fact that a compliance matrix for the layer's upper boundary needs to be formed once and can be used to generate sequences of high fidelity results for varying problem parameters, (v) the avoidance of certain types of numerical difficulties associated with finite elements, which are best described by Hughes (2000), such as element locking. Consistency checks were performed, at the analytical level, to verify the mathematical equivalence between formulations in limiting cases and on overlapping parts of their application domains. In 2D and 3D application examples, the proposed formulations were applied, in combination with appropriate contact solvers (Zéhil and Gavin, 2013a), to illustrate the influence of several parameters on the resistance to motion incurred by rigid cylinders and spheres rolling on compressible isotropic, transversely isotropic and orthotropic layers. In particular, the latter case revealed the existence, at each given speed, of specific directions of motion along which maximum and minimum dissipation occur. This observation may have broader impacts of notable significance, such as on the design and proper orientation of new anisotropic metamaterials, possibly including auxetic components, to optimize the level of damping according to the needs of a given application. For instance, in the strive to achieve more resilient and sustainable infrastructures, higher levels of damping may be sought, in preferential directions, for better earthquake mitigation. Alternatively, low rolling resistance conveyor belts could be produced to reduce industrial power consumption. Similarly, low rolling resistance vehicle tires and road pavements could be designed to limit energy losses and further improve road transport efficiency and vehicle handling. A transverse asymmetry in contact stresses was also noted when the motion takes place at a nonzero angle from the principal axes of orthotropy. In the absence of lateral support, the contact resultant tends to deviate the moving object from its initial course. This observation implies that smooth and 'invisible' guides can be achieved across three-dimensional viscoelastic surfaces by suitable modification of their mechanical properties. Potential fields of impact include vehicle handling, the control of rainwater runoff, the modification of boundary layers in fluid dynamics (with applications to vehicle, watercraft, submarine, aircraft, rocket sled and missile technologies) and the selection of moving components based on speed. The new modeling tools presented in this work stand, as a contribution, to achieving such global goals.

## Acknowledgments

This material is based upon work supported by the National Science Foundation under Grant No. NSF-CMMI-0900324. Any opinions, findings, and conclusions or recommendations expressed in this material are those of the authors and do not necessarily reflect the views of the National Science Foundation.

## References

Boresi, A., Schmidt, R., 2003. Advanced mechanics of materials, 6th Edition. John Wiley & Sons.
URL http://www.wiley.com/WileyCDA/WileyTitle/productCd-0471438812.html

Flom, D. G., Bueche, A. M., 1959. Theory of rolling friction for spheres. Journal of Applied Physics 30 (11), 1725–1730.

Flügge, W., 1975. Viscoelasticity. Springer-Verlag.

Fung, Y., Tong, P., 2001. Classical and Computational Solid Mechanics. Advanced Series in Engineering Science Series. World Scientific.
URL http://www.worldscientific.com/worldscibooks/10.1142/4134

Greenwood, J. A., Tabor, D., 1958. The friction of hard sliders on lubricated rubber: The importance of deformation losses. Proceedings of the Physical Society 71 (6), 989.

Harvey, Jr., P. S., Gavin, H. P., 2013. An experimentally-validated simplified model of a rolling isolation system. Earthquake Engineering and Structural Dynamics Sumbitted.

Hertz, H., 1881. Über die berührung fester elastischer körper (on contact between elastic bodies). Journal für die reine und angewandte Mathematik 92, 156–171.

Hughes, T., 2000. The finite element method: linear static and dynamic finite element analysis. Dover Civil and Mechanical Engineering Series. Dover Publications.
URL http://store.doverpublications.com/0486411818.html

Kalker, J. J., 1979. The computation of three-dimensional rolling contact with dry friction. International Journal for Numerical Methods in Engineering 14 (9), 1293–1307.

Lakes, R., 2009. Viscoelastic Materials. Cambridge University Press.

Lekhnitskiĭ, S., 1963. Theory of elasticity of an anisotropic elastic body. Holden-Day series in mathematical physics. Holden-Day.

Persson, B., 2010. Rolling friction for hard cylinder and sphere on viscoelastic solid. The European Physical Journal E Soft Matter 33 (4), 327–333.

Persson, B. N. J., 2001. Theory of rubber friction and contact mechanics. The Journal of Chemical Physics 115 (8), 3840–3861.
URL http://link.aip.org/link/?JCP/115/3840/1

Pritz, T., 2000. Measurement methods of complex poisson's ratio of viscoelastic materials. Applied Acoustics 60 (3), 279–292.

Qiu, X., 2006. Full two-dimensional model for rolling resistance: hard cylinder on viscoelastic foundation of finite thickness. Journal of Engineering Mechanics 132 (11), 1241–1251.

Qiu, X., 2009. Full two-dimensional model for rolling resistance. ii: Viscoelastic cylinders on rigid ground. Journal of Engineering Mechanics 135 (1), 20–30.

Rand, O., Rovenski, V., Rovenski, V., 2005. Analytical Methods in Anisotropic Elasticity: With Symbolic Computational Tools. Birkhäuser Boston.
URL http://www.springer.com/birkhauser/mathematics/book/978-0-8176-4272-3

Rosa, M., Fortes, M., 1991. Deformation and fracture of cork in tension. Journal of Materials Science 26, 341–348.

Sadd, M., 2009. Elasticity: Theory, Applications, and Numerics. Elsevier Science.
URL http://www.sciencedirect.com/science/book/9780123744463

Slawinski, M., 2010. Waves and Rays in Elastic Continua. World Scientific.
URL http://www.worldscientific.com/worldscibooks/10.1142/7486

Tabor, D., 1955. The mechanism of rolling friction. ii. the elastic range. Proceedings of the Royal Society of London. Series A, Mathematical and Physical Sciences 229 (1177), 198–220.

Vollebregt, E. A. H., June 2012. The Finite Element Method for Solid and Structural Mechanics. VORtech Computing, Delft, The Netherlands.

WorkSafe Technologies, I., 2012. Iso-base platform 2012.
URL http://www.worksafetech.com/

Zéhil, G.-P., Gavin, H. P., 2013a. Simple algorithms for solving steady-state frictional rolling contact problems in two and three dimensions. International Journal of Solids and Structures 50 (6), 843–852.
URL http://www.sciencedirect.com/science/article/pii/S0020768312004921

Zéhil, G.-P., Gavin, H. P., 2013b. Three-dimensional boundary element formulation of a viscoelastic layer of finite thickness applied to the rolling resistance of a rigid sphere. International Journal of Solids and Structures 50 (6), 833–842.
URL http://www.sciencedirect.com/science/article/pii/S002076831200491X